

Ring current and the magnetosphere-ionosphere coupling during the superstorm of 20 November 2003

Y. Ebihara,¹ M.-C. Fok,² S. Sazykin,³ M. F. Thomsen,⁴ M. R. Hairston,⁵ D. S. Evans,⁶ F. J. Rich,⁷ and M. Ejiri¹

Received 29 November 2004; revised 23 February 2005; accepted 8 April 2005; published 11 August 2005.

[1] We investigated the impact on the terrestrial ring current of a coronal mass ejection (CME) and the associated magnetic cloud that severely disturbed the Earth's magnetosphere on 20 November 2003. This CME decreased the *Dst* index to -472 nT, which makes it the second largest storm, based on the minimum *Dst* index values, observed between 1957 and 2004. Data from the DMSP, NOAA, and LANL satellites showed the unique characteristics of this storm; a polar cap potential that increased to at least 200 kV, a polar cap boundary that moved as low as about 60° MLAT, a plasma sheet density that increased to 5 cm^{-3} at $L = 6.6$ when the *Dst* index was near its minimum, and the inner edge of the plasma sheet ion population that penetrated into a region for which $L \leq 1.5$. In order to study the dynamics of the ring current and the associated magnetosphere-ionosphere coupling, we performed a ring current simulation that computed the evolution of the phase space density of the ring current ions and the closure of the electric current between the magnetosphere and the ionosphere. Major results were as follows: (1) The ring current, in terms of the *Dst* index and the inner edge of the plasma sheet, can result from the enhancement of the convection electric field, given the polar cap potentials used in the model; (2) The solar wind particles probably penetrated quickly into the geosynchronous altitude on the nightside with a lag of about 80 min, resulting in further enhancement of the ring current; (3) Dense geocoronal neutral hydrogen or a large coefficient of pitch angle diffusion ($>10^{-4}\text{ s}^{-1}$) is probably needed to account for the rapid motion of the inner edge of the plasma sheet (or the ring current) population to a higher L value; (4) Both the simulated and observed field-aligned current (FAC) distributions show multiple current sheets, rather than the normally expected two current sheets. Fluctuations in the polar cap potential and the plasma sheet density are believed to cause the multiple sheets of field-aligned currents; (5) The equatorward edge of the Region 2 type field-aligned currents was observed to expand as low as 40° MLAT, which is consistent with the simulation; and (6) The convection pattern can be much more complicated than an average one due to a strong Region 2 FAC. A noticeable feature was the reversal of the zonal ionospheric plasma flow that emerged on the dawnside. In particular, a westward flow was observed in the equatorial region of the eastward plasma flow at dawn. Its speed had a local maximum of about 5° equatorward of the flow reversal. The flow reversal is thought to have resulted from the relatively strong shielding electric field.

Citation: Ebihara, Y., M.-C. Fok, S. Sazykin, M. F. Thomsen, M. R. Hairston, D. S. Evans, F. J. Rich, and M. Ejiri (2005), Ring current and the magnetosphere-ionosphere coupling during the superstorm of 20 November 2003, *J. Geophys. Res.*, 110, A09S22, doi:10.1029/2004JA010924.

¹National Institute of Polar Research, Tokyo, Japan.

²NASA Goddard Space Flight Center, Greenbelt, Maryland, USA.

³Physics and Astronomy Department, Rice University, Houston, Texas, USA.

⁴Los Alamos National Laboratory, Los Alamos, New Mexico, USA.

⁵Center for Space Science, University of Texas at Dallas, Richardson, Texas, USA.

⁶NOAA Space Environment Laboratory, Boulder, Colorado, USA.

⁷Air Force Research Laboratory, Hanscom Air Force Base, Massachusetts, USA.

1. Introduction

[2] A halo coronal mass ejection (CME) associated with an M-class solar flare occurred on 18 November 2003. The leading edge of the CME, accompanied by high-speed solar winds reaching ~ 700 km/s and a strong southward component of the interplanetary magnetic field (IMF) reaching ~ 60 nT at 1 AU, struck the Earth's magnetosphere on 20 November 2003. Table 1 summarizes previous superstorms with minimum *Dst* reaching -300 nT or less that occurred between 1957 and 2004. A total of 22 such

Table 1. List of Superstorms (Minimum $Dst < -300$ nT) Between 1957 and 2004

Year	Month	Day	UT	Minimum Dst
1989	3	14	0100	-589
2003	11	20	1900	-472 ^a
1959	7	15	1900	-429
1957	9	13	1000	-427
1958	2	11	1100	-426
2003	10	30	2200	-401 ^a
2001	3	31	0800	-387
1967	5	26	0400	-387
2004	11	8	0600	-373 ^a
2003	10	30	0000	-363 ^a
1991	11	9	0100	-354
1960	11	13	0900	-339
1958	7	8	2200	-330
1960	4	1	1800	-327
1982	7	14	0100	-325
1960	4	30	1800	-325
1957	9	5	0300	-324
1981	4	13	0600	-311
1986	2	9	0000	-307
1957	9	23	0700	-303
1958	9	4	2200	-302
2000	7	16	0000	-301

^aProvisional Dst .

superstorms were recorded. The largest storm was the March 1989 storm with a minimum Dst reaching -589 nT. During the 20 November 2003 storm, the minimum provisional Dst index was -472 nT, which makes this storm the second largest disturbance in the table.

[3] We expect that a large amount of energy accumulated in the inner magnetosphere during the November 2003 storm. In order to continuously accumulate this amount of energy in the inner magnetosphere, two prime sources need to be present. The first source is an enhanced convection electric field which drives the ring current ions electrically. The second source is an enhanced plasma sheet density that is the origin of the ring current ions. A strong convection electric field is capable of pushing the ions originating from the nightside plasma sheet deep into the inner region where the Earth's magnetic field is stronger. Thus these ions gain kinetic energy as they drift toward the Earth, since they must conserve the first and second invariants. Consequently, the energy density near the inner edge of the plasma sheet is usually larger than that found in the outer region. The second possible source is the high plasma sheet density, which has been postulated by *Chen et al.* [1994], *Jordanova et al.* [1998], *Kozyra et al.* [1998b], and *Ebihara and Ejiri* [1998, 2000]. *Jordanova et al.* [1998] simulated the October 1995 storm that exhibited two minimal Dst values. They concluded that the second minimum Dst value was caused by an increase in the plasma sheet density to 5 cm^{-3} .

[4] As a result of the accumulation of particle energy, a strong electric current (ring current) flows perpendicularly to a magnetic field line and can be monitored using ground magnetograms. An electric current parallel to the magnetic field line also flows when the divergence of the perpendicular electric current is nonzero. On average, the field-aligned current (FAC) resulting from the ring current tends to flow into the ionosphere on the duskside and away from the ionosphere on the dawnside [*Zmuda and Armstrong*, 1974; *Iijima and Potemra*, 1976].

[5] To remove the space charge deposited by the FACs, Pedersen currents are established in the ionosphere. The associated electric field is usually directed toward the east on the nightside when the net FAC flows into the ionosphere on the duskside and away from the ionosphere on the dawnside. The eastward directed electric field is opposite the direction of the convection electric field, which is usually directed toward the west on the nightside. Therefore the additional electric field is called a shielding electric field because it tends to cancel out the convection electric field. The consequent potential pattern of the ionospheric electric field is highly distorted by the presence of the FACs and the corresponding shielding field (see *Harel et al.* [1981] and *Toffoletto et al.* [2003] for review).

[6] It should be mentioned that numerous simulations of the ring current have been carried out for a number of magnetic storms; those of February 1986 [*Kozyra et al.*, 1998a; *Khazanov et al.*, 2003b], May 1986 [*Fok and Moore*, 1997; *Fok et al.*, 2001], June 1991 [*Liemohn et al.*, 1999, 2002a; *Kozyra et al.*, 2002; *Garner et al.*, 2004], August 1991 [*Chen et al.*, 1999], November 1993 [*Kozyra et al.*, 1998b], October 1995 [*Jordanova et al.*, 1998], March 1996 [*Jordanova et al.*, 1999a], January 1997 [*Jordanova et al.*, 1999b, 2003], April 1997 [*Ebihara and Ejiri*, 2000], May 1997 [*Jordanova et al.*, 2001a; *Liemohn et al.*, 2001, 2002a], March 1998 [*Jordanova et al.*, 2001b], May 1998 [*Khazanov et al.*, 2003a], September 1998 [*Liemohn et al.*, 1999, 2001, 2002a; *Sazykin et al.*, 2002], October 1998 [*Liemohn et al.*, 2001, 2002a], July 2000 [*Jordanova et al.*, 2001c; *Liemohn et al.*, 2002b], and August 2000 [*Fok et al.*, 2003; *Ebihara et al.*, 2004]. However, all the above storms were weaker than the November 2003 storm in terms of the minimum Dst value. Thus this paper considers: (1) the response of the ring current to the extreme condition of the IMF and the solar wind; and (2) the electrodynamics caused by the strong ring current during the extreme magnetospheric condition, both of which have not been previously simulated.

[7] There was no continuous observation of the IMF and the solar wind during the March 1989 storm, which was the largest storm between 1957 and 2004. This lack of information limits our ability to simulate the ring current. Also, no reliable measurements of the solar wind were made during the October 2003 superstorms, which were the sixth and tenth largest storms between 1957 and 2004, since the particle detectors on board the ACE satellite were damaged by the intense solar energetic protons associated with major solar flares. However, during the November 2003 storm, the IMF and solar wind were continuously monitored by numerous satellites in various magnetospheric regions. This information enabled us to examine how the ring current responded to the unusual variation of the IMF and the solar wind and its coupling with the ionosphere.

[8] We investigated the development of the ring current and the consequence of the electric coupling between the magnetosphere and the ionosphere during the superstorm by using data from the ACE satellite that provided the IMF and solar wind data; the LANL satellites that provided the plasma sheet density and temperature data at $L = 6.6$; the NOAA satellite that provided the trapped ion flux data; and the DMSP satellites that provided the magnetic deflection due to FACs and the ionospheric plasma drift data. In order

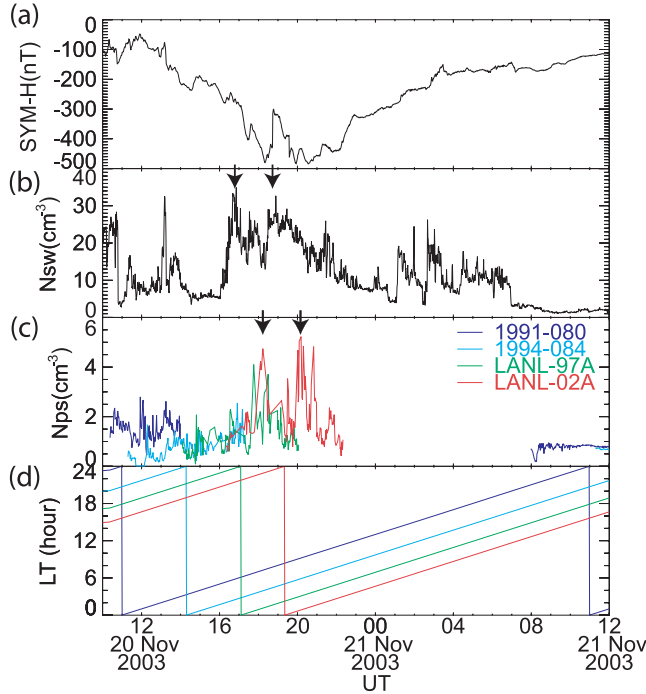


Figure 1. (a) The SYM index, (b) the solar wind density N_{sw} measured by ACE, (c) the plasma sheet density N_{ps} measured by the LANL satellites (1991-080, 1994-084, LANL-97A and LANL-02A) in the nightside sector at $L = 6.6$, and (d) the local time of the LANL satellites. The N_{sw} variation is shifted by 40 min to take into account the propagation time between ACE and the magnetosphere.

to explain the observations, we performed a numerical simulation that solved the spatial-temporal evolution of the ring current ion distribution and the electric potential distribution driven by the ring current. We focused on the following four features: the variation in the Dst values; the penetration of the plasma sheet (ring current) ions; the field-aligned current generated by the ring current; and the ionospheric flow reversal seen at dawn.

2. Observation

2.1. Plasma Sheet Density

[9] Figure 1 shows the plasma sheet density, N_{ps} (0.1–40 keV), measured by the Magnetospheric Plasma Analyzer (MPA) [McComas *et al.*, 1993] on board the four LANL satellites (1991-080, 1994-084, LANL-97A, and LANL-02A) at $L = 6.6$ on the nightside sector between 2100 MLT and 0300 MLT, together with the solar wind density, N_{sw} , measured by the ACE satellite at distance of $230 R_E$ from the subsolar point of the magnetopause. Assuming a constant solar wind speed of 600 km/s, we shifted the solar wind density, N_{sw} , by 40 min to take into account the propagation time from the ACE satellite to the magnetosphere. At least one of the LANL satellites measuring N_{ps} covered the nightside sector during the main phase of the storm between ~ 1200 and ~ 2000 UT on 20 November. There are two noticeable peaks in the value of N_{ps} . The first peak occurred at around 1800 UT, while the second peak occurred at around 2000 UT on 20 November 2003. The

first peak, which resulted in an increase of the density from $\sim 1\text{--}2 \text{ cm}^{-3}$ to $\sim 4\text{--}5 \text{ cm}^{-3}$ at around 1800 UT, was simultaneously detected by the two LANL satellites of LANL-97A and LANL-02A. LANL-97A was located in the postmidnight sector, while LANL-02A was located in the premidnight sector. This suggests that N_{ps} increased almost simultaneously in the wide region spanning at least ~ 2100 MLT to ~ 0200 MLT where the two LANL satellites were located. After this interval, LANL-97A moved away from the nightside sector at ~ 2000 UT and the spatial extent of the second N_{ps} peak are unknown.

[10] As shown in Figure 1b, a similar double peak occurred in the solar wind density, N_{sw} , around 1730 UT and 1930 UT. Assuming that the double peak behavior of the N_{ps} is associated with the double peak behavior of the N_{sw} , the best cross-correlation coefficient between N_{ps} and the time-shifted N_{sw} is 0.31 for a time delay of 80 min. Despite the uncertainty associated with solar wind propagation from the ACE satellite to the magnetosphere, the estimated time delay of 80 min is much shorter than that suggested for the November 1993 storm, for which Borovsky *et al.* [1998] suggested that the solar wind material reached the near-Earth nightside plasma sheet at $L = 6.6$ in about 4 hours. The low correlation coefficient of 0.31 suggests that the transport processes of the solar wind to the magnetosphere are not as simple as expected.

2.2. Polar Cap Potential and Polar Cap Boundary

[11] Figure 2 shows the polar cap potential drops (PCPs) derived from the ion drift data from the DMSP F13 satellite and estimated using three empirical models. The measured PCP, indicated with a red line, increased to about 200 kV during the main phase. The sawtooth-like fluctuation between 1200 UT on 20 November and 0000 UT on 21 November reflects the difference between the Northern and Southern Hemispheres. It should be noted that the DMSP F13 satellite flew along the dawn-dusk meridian but did not always pass through the minimum and maximum electric potentials. The DMSP measurements give an estimate for the lower limit of the PCP.

[12] The three calculated PCP tracings are overlaid in Figure 2a. They were calculated using the models presented by Boyle *et al.* [1997] (black), Weimer *et al.* [2001] (green), and Hill-Siscoe-Ober [Hill *et al.*, 1976; Siscoe *et al.*, 2002; Ober *et al.*, 2003]. The solar wind and the IMF data from the ACE satellite were used to calculate the PCP. The solar wind parameters were shifted by 40 min to take into account the propagation time from the ACE satellite to the magnetosphere.

[13] The model presented by Boyle *et al.* [1997] predicts the PCP using the following expression:

$$\Phi_{PCP}(\text{kV}) = 1.1 \times 10^{-4} V_{sw}^2 + 11.1 B_{IMF} \sin^3(\theta_{IMF}/2),$$

where V_{sw} is the solar wind velocity in km/s, B_{IMF} is the magnitude of the IMF in nT, and θ_{IMF} is the clock angle of the IMF. This model predicted PCP values exceeding 650 kV, which are higher than those observed. As suggested by Ober *et al.* [2003], this overestimation is probably due to the fact that the model presented by Boyle *et al.* [1997] was constructed from data acquired during quiet or moderately active periods.

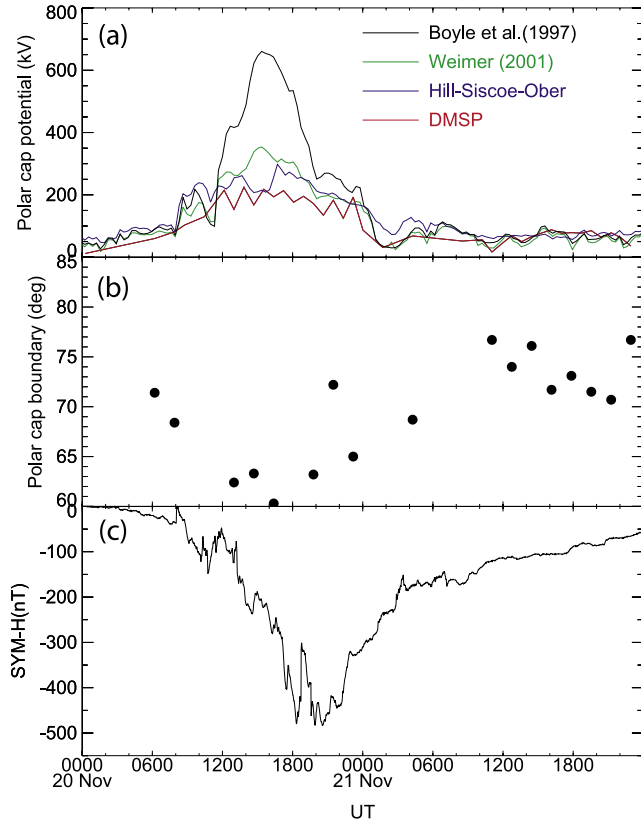


Figure 2. (a) Polar cap potential drops calculated by Boyle *et al.* [1997] (black), Weimer [2001] (green), Hill-Siscoe-Ober [Hill *et al.*, 1976; Siscoe *et al.*, 2002; Ober *et al.*, 2003] (blue) models, together with that from DMSP F13 (red), (b) the polar cap boundary measured by the ion drift meter on-board DMSP F13, and (c) the SYM-H index.

[14] The empirical model of Weimer *et al.* [2001] predicts that the PCP is proportional to $B_T^{2/3}$, where B_T is the tangential component of the IMF. The nonlinear term results in PCPs that are much smaller than those predicted by the model of Boyle *et al.* [1997] when the component of the IMF in the southern direction is strong. The Weimer *et al.* [2001] model predicts a maximum value of 360 kV, while the Hill-Siscoe-Ober model predicts a maximum value of 300 kV.

[15] The Hill-Siscoe-Ober model takes into account the saturation behavior of the PCP for a high solar wind electric field and predicts PCPs that are close to observational values. Similar agreement with the observational values was also reported for the March 2001 storm [Hairston *et al.*, 2003; Ober *et al.*, 2003]. As described below, we used the PCP predicted by the Hill-Siscoe-Ober model in the simulation.

[16] The DMSP F13 measurements can be also used to estimate the polar cap boundary (PCB) latitude. The PCB measured in the Northern Hemisphere is shown in Figure 2b. The lowest latitude of the PCBs determined in the dawnside and duskside is plotted. The PCB latitude decrease preceded the storm's main phase and reached an unusually low value of 60° MLAT at ~1600 UT on 20 November. In addition to the enhancement of the PCP, the expansion of

the PCB should increase the net magnetospheric convection electric field in the entire inner magnetosphere because the inner magnetosphere shrinks when the PCB latitude decreases.

3. Simulation

[17] We simulated this superstorm using the Comprehensive Ring Current Model [Fok *et al.*, 2001]. This simulation solves the kinetic equation of the ring current particles and the closure of the electric current between the magnetosphere and ionosphere. Assuming that the first two invariants are conserved, we solved the particle transport under the bounce-averaged approximation as

$$\frac{\partial \bar{f}_s}{\partial t} + \langle \dot{\lambda}_i \rangle \frac{\partial \bar{f}_s}{\partial \lambda_i} + \langle \dot{\phi}_i \rangle \frac{\partial \bar{f}_s}{\partial \phi_i} = -v \sigma_s \langle n_H \rangle \bar{f}_s - \left(\frac{\bar{f}_s}{0.5 \tau_b} \right)_{\text{loss cone}}, \quad (1)$$

where $\bar{f}_s = \bar{f}_s(\lambda_i, \phi_i, M, K)$ is the four-dimensional phase space density, M is the first invariant, K is the second invariant, λ_i is the magnetic latitude of the ionospheric altitude, ϕ_i is the magnetic longitude, v is the particle velocity, σ_H is the cross section for charge exchange, n_H is the hydrogen density, and τ_b is the bounce period. The angle brackets stand for a quantity bounce-averaged over a field line between two mirror points. The absorption altitude for the loss cone was defined to be 100 km.

[18] The bounce-averaged drift motion of the particles was solved in terms of the four-dimensional phase space density specified by the latitude (λ_i), MLT (ϕ_i), the first invariant (M), and the second invariant (K). The spatial coordinates were fixed at the ionospheric altitude. The particle transport was computed in the region below the poleward particle boundary, λ_1 , set to a constant value of 67.6° in this particular simulation. The phase space density specified in the M - K space can be easily mapped to the energy-and-equatorial-pitch-angle space that is convenient for comparison with the satellite observations.

[19] Continuous measurements of the N_{ps} and the T_{ps} by the LANL satellites at $L = 6.6$ were used to determine the boundary condition in this simulation. When two or more LANL satellites covered the nightside sector ranging between 2100 MLT and 0300 MLT, we took into consideration all the satellites present in determining the values of N_{ps} and T_{ps} . When only one LANL satellite was available in the nightside sector, we assumed that N_{ps} and T_{ps} were distributed uniformly in the MLT. When no LANL satellite was available, we interpolated N_{ps} and T_{ps} based on the two most recent observations. The LANL observations were made at 6.6 R_E , which is closer to the Earth than our poleward particle boundary, λ_1 , when we mapped to the equatorial plane. Therefore we simply mapped the phase space density from 6.6 R_E to λ_1 in accordance with the Liouville theorem to obtain the boundary condition in the simulation.

[20] We assumed that all the ions consisted of protons and that the distribution function of the protons at $L = 6.6$ was an isotropic Maxwellian distribution. The magnetosphere was assumed to be initially filled with preexisting particles having the distribution function measured by the AMPTE/CCE satellites during quiet time [Sheldon and Hamilton,

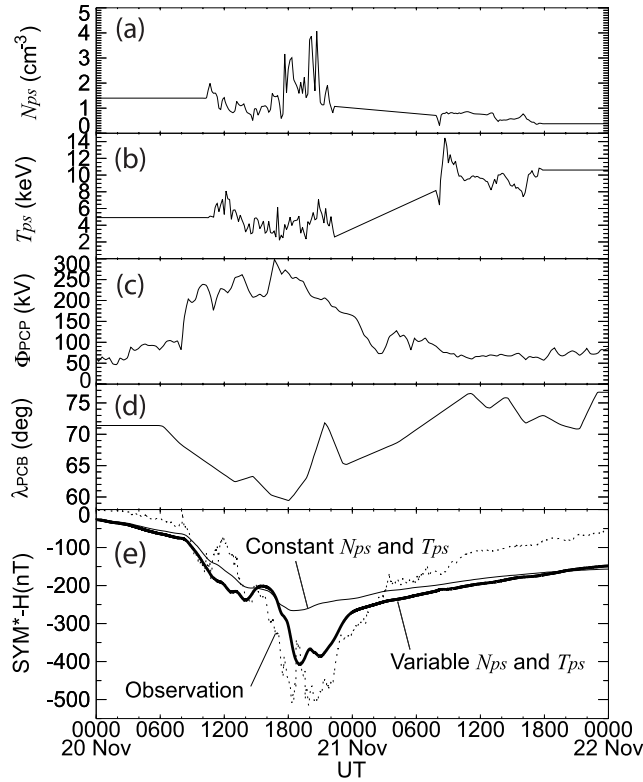


Figure 3. (a) The plasma sheet density N_{ps} at $L = 6.6$ at midnight, (b) the plasma sheet temperature T_{ps} at $L = 6.6$ at midnight, (c) the polar cap potential drop Φ_{PCP} , (d) the magnetic latitude of the polar cap potential drop λ_{PCB} , and (e) observed SYM*-H (dashed line) and simulated SYM*-H (thick solid line). The thin solid line represents the simulated SYM*-H values using constant N_{ps} and T_{ps} values for the boundary conditions. The first four parameters were the input parameter for the simulation.

1993]. The distribution function of the preexisting particles does not significantly affect the result because the preexisting particles will be lost soon after the enhancement of the convection electric field as the newly injected particles occupy the inner magnetosphere.

[21] The magnetospheric protons were lost by two processes in this simulation. One process involved adiabatic loss cone loss. The other process involved charge exchange with neutral hydrogen, the so-called geocorona. The neutral hydrogen density was calculated using the *Chamberlain* [1963] model with its parameter given by *Rairden et al.* [1986].

[22] We solved the following Poisson equation to obtain the electric potential distribution at an ionosphere altitude of 100 km,

$$\nabla \cdot (-\Sigma \cdot \nabla \Phi) = -j_{\parallel} \sin I, \quad (2)$$

where Σ is the conductivity tensor, Φ is the electric potential, j_{\parallel} is the field-aligned current density, and I is the inclination of the magnetic field. The electric potential distribution was solved in the latitude region below the

poleward potential boundary, λ_2 , where the polar cap potential was imposed as

$$\Phi(\phi_i, \lambda_i = \lambda_2) = \Phi_{PCP} \sin \phi_i. \quad (3)$$

The poleward potential boundary, λ_2 , was treated as a variable in order to simulate the equatorward expansion of the polar cap boundary (PCB), while the poleward particle boundary, λ_1 , was treated as a constant. Under quiet conditions, the polar cap boundary PCP is usually located above λ_1 , which was set to 67.6° in this simulation. We set $\lambda_2 = \lambda_1$ when $\lambda_{PCB} > \lambda_1$, where λ_{PCB} is the PCB latitude observed by DMSP F13. This may have resulted in a slight overestimation of the electric field under quiet conditions, when $\lambda_{PCB} > \lambda_1$. In a disturbed condition, the PCB is expanded, and may be located equatorward of the λ_1 . We set $\lambda_2 = \lambda_{PCB}$ when $\lambda_{PCB} < \lambda_1$. The gap between λ_1 and λ_2 was filled with the electric potential given by

$$\Phi(\phi_i, \lambda_2 < \lambda_i < \lambda_1) = \Phi_{PCP} \sin \phi_i. \quad (4)$$

The electric potential at the ionospheric altitude was immediately mapped to the magnetosphere along a field line by assuming that the field line is equipotential. The newly updated electric field alters the particle drift motion. Therefore the simulation system is essentially nonlinear.

[23] The total ionospheric conductance tensor Σ is the sum of the solar EUV origin and the auroral particle origin. The International Reference Ionosphere (IRI-95) [Bilitza, 1997] and the Mass Spectrometer Incoherent Scatter (MSIS-E90) models [Hedin, 1991] were employed to calculate the background conductance due to the solar EUV. Since our model does not follow the plasma sheet electrons and does not include any auroral (discrete) precipitating feature, we used the *Kp*-dependent empirical model of *Hardy et al.* [1987] to calculate the contribution to conductance from the precipitating auroral electrons.

[24] We used the T96 empirical magnetic field model [Tsyganenko, 1995; Tsyganenko and Stern, 1996] to define the external magnetic field parameterized by the solar wind dynamic pressure, the *Dst* index, and the IMF B_y and B_z . On the basis of the observations made at the beginning of the simulation (0000 UT on 20 November 2003), the following input parameters were selected for the T96 model: a solar wind dynamic pressure of 1.44 nPa, a *Dst* value of -8 nT, an IMF B_y value of 4.3 nT, and an IMF B_z value of 1.3 nT. The magnetic field was kept constant over time. We believe that the choice of the static and quiet-time magnetic field model does not significantly affect the most results, since our primary focus was on the inner region ($L < 3$) where the dipolar magnetic field dominates. The radial transport of magnetospheric ions with energy between a few keV and a few hundreds of keV is governed by the $E \times B$ drift in the simulation. The magnetic field distribution may be less important for the radial transport of the ions of interest than the electric field distribution.

4. Results

4.1. *Dst* (SYM*-H)

[25] Figure 3 displays the input parameters used in the simulation: (1) N_{ps} at $L = 6.6$ at midnight, (2) T_{ps} at $L = 6.6$

at midnight, (3) Φ_{PCB} and (4) λ_{PCB} . The calculated SYM*-H is shown in Figure 3e with a solid line, together with the observed values indicated by a dotted line. SYM*-H, the 1-min SYM index corrected to the solar wind dynamic pressure, is used as a proxy of the 1-hour Dst^* index and is given by

$$\text{SYM}^* - H = \text{SYM} - H - c_1 P_{sw}^{1/2} + c_2, \quad (5)$$

where P_{sw} is the solar wind dynamic pressure and c_1 and c_2 are empirical coefficients. We assumed that c_1 had a value of $0.2 \text{ nT}/(\text{eV cm}^{-3})^{1/2}$ and c_2 had a value of 20 nT [Gonzalez et al., 1994]. In the simulation, the SYM*-H was calculated using the Dessler-Parker-Sckopke relationship [Dessler and Parker, 1959; Sckopke, 1966], which states that the magnetic deflection at the center of the Earth is proportional to the total particle energy, that is,

$$\text{SYM}^* - H(\text{nT}) = -2.495 \times 10^{-14} \varepsilon(J), \quad (6)$$

where ε is the total particle energy accumulated in the simulation region. The effect of Earth's induction was considered by multiplying the modeled SYM*-H by a factor of 1.5 [Dessler and Parker, 1959].

[26] The calculated SYM*-H variation was found to be in general agreement with the observed variation. The simulated SYM*-H reached its minimum of -408 nT , while the observed SYM*-H reached a minimum of -516 nT . This difference may be in part attributed to contributions from current systems other than the ring current. The possible current systems affecting SYM*-H are the tail current, the field-aligned current, and the ionospheric current. A quantitative comparison of the observed and simulated SYM*-H values is beyond the scope of interest as it is difficult to exclude the contributions from other current systems.

[27] Of interest, double dips were noted in the observed SYM*-H at 1820 UT and 1956 UT. The simulated SYM*-H also exhibited double dips at 1900 UT and 2057 UT on 20 November due to the double peak in N_{ps} (thick solid line). We repeated the same simulation with N_{ps} held constant to 1.0 cm^{-3} and T_{ps} held constant to 5 keV , so as to be consistent with the averaged values at the geosynchronous altitude [Thomsen et al., 1996]. When N_{ps} and T_{ps} are held constant, the double dips in SYM*-H become a single dip as indicated with a thin solid line in Figure 3e.

[28] By comparing the two curves of the calculated SYM*-H (one time-dependent and the other a time-independent boundary condition) shown in Figure 3e, the abrupt decay of N_{ps} is recognized to result in a rapid recovery of SYM*-H. This agrees with the actual observed data. An abrupt decay in the value of N_{ps} has been suggested as necessary, in many cases, to explain the rapid recovery of Dst^* [Kozyra et al., 1998b; Jordanova et al., 1998; Ebihara and Ejiri, 1998, 2000]. Recently, Sazykin et al. [2002] have pointed out that an abrupt decay in the value of N_{ps} leads not only to the rapid recovery of Dst^* but interchange instability when the ring current is coupled with the ionosphere.

[29] This interchange instability is expected to be present in this superstorm because N_{ps} decreases suddenly. When N_{ps} decreases suddenly, the outer plasma sheet becomes

tenuous, while the inner plasma sheet remains dense because of the sunward convection electric field. Some perturbations of the plasma pressure, which can be caused by the time-dependent convection electric field and N_{ps} , generate field-aligned currents. To remove space charges deposited by the field-aligned currents, Pedersen currents have to develop in the ionosphere. The additional electric field tends to increase the magnitude of the perturbations. Owing to this instability, the interface between the dense and tenuous plasma sheet shows large-scale undulations and the electric potential distribution becomes complicated, as shown in Figure 4. Sazykin et al. [2002] have reviewed this in more detail. The plasma pressure distribution distorted by the interchange instability may result in the complicated distribution of the field-aligned currents as mentioned in section 4.3.

4.2. Deep Penetration of Plasma Sheet Ions

[30] Figure 5 includes an L versus time (L - t) diagram of the flux of 30–80 keV ions measured by the polar-orbiting NOAA 17 satellite near the 2200 MLT meridian, indicating that the inner edge of the ion plasma sheet gradually moved inward during the main phase (Figure 5b). The flux was measured by a detector pointing toward the horizon, corresponding to the trapped particle flux at high latitudes (high L values) where the inclination of a geomagnetic field line is large. The inner edge eventually reached as deep as $L = 1.5$ at around 1900 UT on 20 November 2003. This penetration of the plasma sheet is much deeper than during the 4–5 June 1991 storm [Garner et al., 2004]. During the recovery phase, the inner edge tends to retreat to a higher L value, according to data from the NOAA 17 satellite. However, it should be noted that the rapid retreat observed between 1900 UT on 20 November and 0300 UT on 21 November is partly due to a geographic effect. The intensity of the flux depends largely on the local geomagnetic field strength that determines the loss cone angle of the trapped particles. The magnetic field strength at the NOAA-17 altitude has significant geographic longitude dependence for any given L value.

[31] Figure 5c shows the L - t diagram of the simulated proton fluxes at the 2200 MLT meridian. A pitch angle of 90° at 830 km altitude, which corresponds to the NOAA 17 satellite's altitude, was chosen as the comparison basis for the NOAA 17 observations. The inner edge of the plasma sheet gradually moved toward the Earth during the main phase. The inner edge of the plasma sheet reached $L = 1.5$ at about 1200 UT on 20 November, which is fairly consistent with the NOAA 17 data. This agreement indicates that the strong convection electric field with the polar cap potential drop predicted by the Hill-Siscoe-Ober model is capable of pushing the plasma sheet particles deeply for an L value of 1.5.

[32] When focusing on the recovery phase, one sees a disagreement between the observed and simulated innermost location of the ion population extending from the high L value. The observed boundary shows a rapid retreat antiearthward as compared with the simulated one. The plasma sheet density N_{ps} decreased during the early recovery phase, but the abrupt decrease in N_{ps} does not account for the rapid retreat. Loss processes, other than the traditional charge exchange loss, may be needed to account for

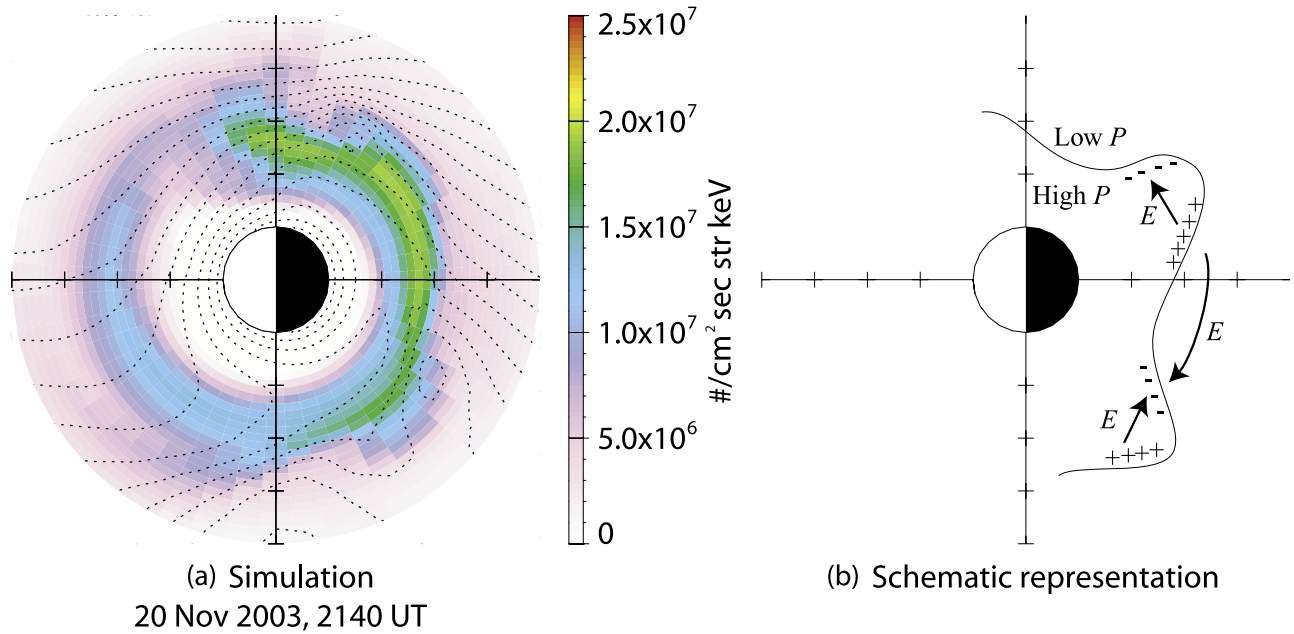


Figure 4. (a) Calculated differential flux with an energy of 32 keV and an equatorial pitch angle of 60° in the equatorial plane at 2140 UT on 20 November 2003 just after N_{ps} starts decreasing, and (b) schematic representation of the possible interchange instability on the nightside. The simulated electric potential including the corotation field is overlaid on the left.

the rapid poleward motion to the higher L values of this boundary.

[33] There are several explanations for the disagreement. First, the dense neutral hydrogen in the inner magnetosphere could shorten the lifetime of the protons due to charge exchange. Second, pitch angle scattering could become significant and increase the loss of particles into the upper atmosphere. Third, dense plasmaspheric electrons could shorten the lifetime of the ring current protons due to Coulomb collisions. Fourth, the ion composition could be dominated by oxygen, whose charge exchange lifetime is slightly shorter than for hydrogen ions with energy greater than about 40 keV.

[34] Figure 6 shows the simulation results calculated under the conditions that (1) the neutral hydrogen density is 5 times higher than modeled by *Rairden et al.* [1986]; (2) the neutral hydrogen density is 10 times higher; (3) the pitch angle diffusion occurs with a diffusion coefficient, $D_{\alpha\alpha}$, of 10^{-5} s^{-1} ; (4) the pitch angle diffusion coefficient, $D_{\alpha\alpha}$, is 10^{-4} s^{-1} ; and (5) the diffusion coefficient, $D_{\alpha\alpha}$, is 10^{-3} s^{-1} . As well, we assumed that pitch angle diffusion occurs everywhere independent of the energy and equatorial pitch angle. The calculated L - t diagram for the 30–80 keV proton flux shows a retreat of the inner edge of the plasma sheet when the neutral hydrogen density is 5 or 10 times higher than that modeled by *Rairden et al.* [1986] (Figures 6a and 6b), or when the pitch angle diffusion coefficient is 10^{-4} s^{-1} or larger (Figures 6c and 6d).

[35] No evidence, however, has been provided to demonstrate that the neutral hydrogen density was increased by a factor of 5 or more for this particular storm. Thermal escape fluxes of the neutral hydrogen from the exobase (Jeans escape) were calculated to increase from 4×10^7 to $1 \times 10^8 \text{ cm}^{-2} \text{ s}^{-1}$ when the exospheric temperature

increased from 1000 K to 1400 K [Bertaux, 1975]. The amount of hydrogen in the high-energy tail of the Maxwellian distribution at the exobase increases with the exospheric temperature, and thus the geocoronal hydrogen density decreases. The exospheric temperature was apparently high during the superstorm, and hence it is unlikely to attribute the increase in the neutral hydrogen density to the exospheric temperature.

[36] According to a Monte Carlo simulation of the geocoronal hydrogen, for the solar maximum (minimum) condition, when the plasmasphere is empty, hydrogen density is higher by about 25% (40%) than when the plasmasphere is filled [Tinsley et al., 1986]. The plasmasphere is the sink for the neutral hydrogen through the charge exchange process with plasmaspheric thermal ions. When the plasmasphere is filled, the charge exchange process occurs more frequently, thus decreasing the neutral hydrogen density. During the superstorm, the plasmapause could be shrunk by the large-scale convection electric field, and thus an increase in the neutral hydrogen density outside of the plasmapause could occur. The increase in the neutral hydrogen enhances the charge exchange rate of the ring current ions with the neutral hydrogen. Our static neutral hydrogen model is unable to solve the dynamic behavior of neutral hydrogen. In the future, a simulation that takes into account the dynamic model of neutral hydrogen should be done to quantitatively analyze the influence of the plasmasphere on the decay of the ring current through the charge exchange process.

[37] Observations have shown that oxygen ions (with energy between 50 and 400 keV) sometimes dominate the ion composition during large storms [Daglis, 1997]. If the ion composition is dominated by oxygen, then the charge exchange lifetime will be different from that when hydrogen

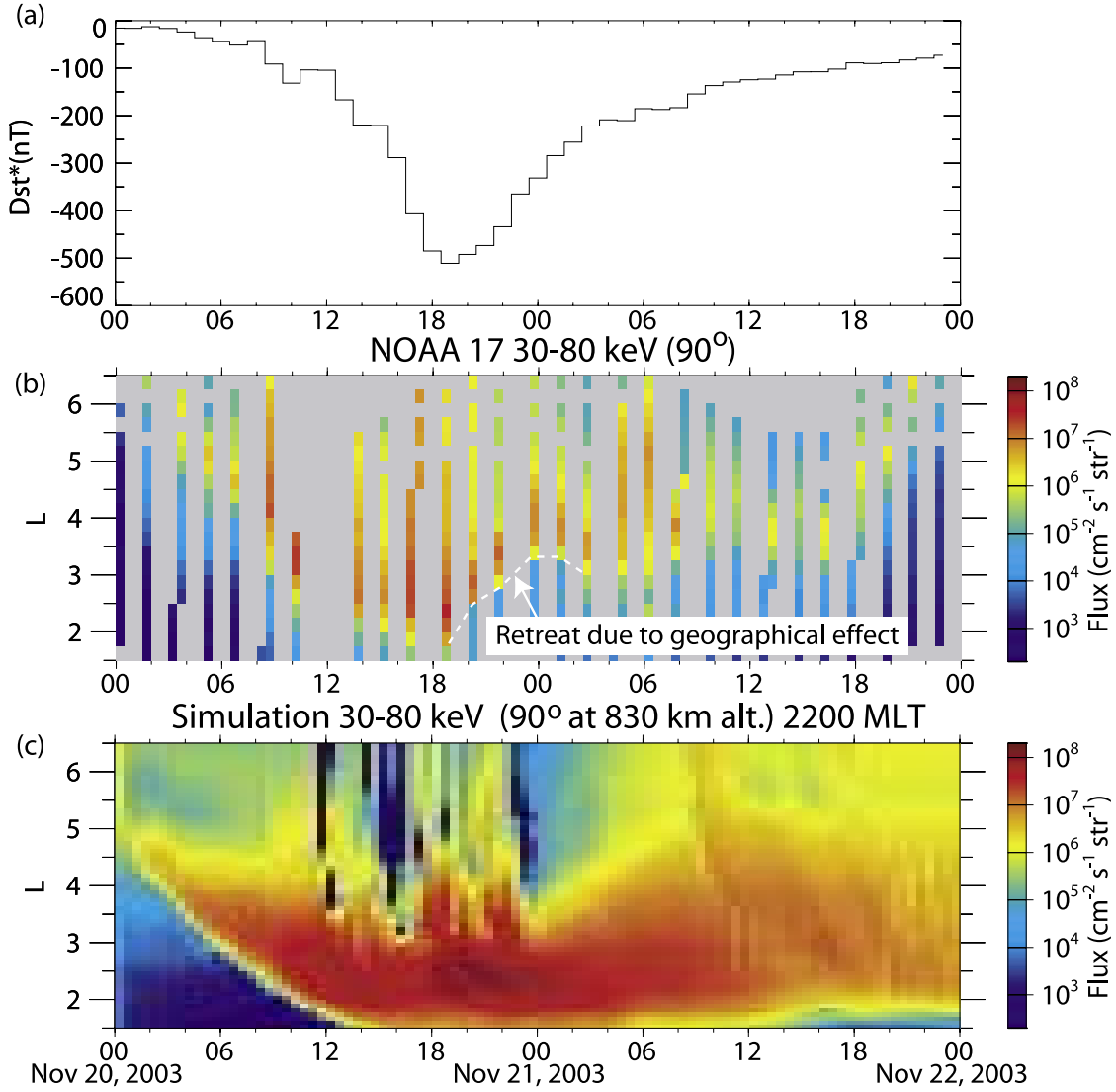


Figure 5. (a) Dst*, (b) ion flux observed by NOAA 17 with the detector pointing toward the horizon with energies between 30 and 80 keV in the Northern Hemisphere in the evening sector, and (c) simulated proton flux at 2200 MLT meridian with energy between 30 and 80 keV with pitch angle of 90° at an altitude of 830 km. Note that there is a data gap in the NOAA 17 data around 1200 UT on 20 November 2003.

ions dominate. For high-energy ions the lifetime of oxygen is shorter than that of hydrogen, while for low-energy ions it is longer than that of hydrogen. The transition occurs at about 40 keV [c.f. Ebihara and Ejiri, 2003, Figure 5]. We repeated the same simulation with an ion composition completely dominated by oxygen. The result shows that the location of the low L value boundary of the oxygen population with 30–80 keV did not retreat as fast as observed (data not shown). The charge exchange seen with the averaged neutral density is unlikely to account for the rapid recovery noted, even though the ions are dominated by oxygen.

[38] If the pitch angle diffusion can explain the discrepancy between simulated and observed values, then a relatively large diffusion coefficient, $D_{\alpha\alpha}$, of $\sim 10^{-4} \text{ s}^{-1}$ or greater, is needed to account for the NOAA 17 observation as shown in Figure 6. As described by Kennel [1969], strong

diffusion occurs when a bounce-averaged pitch angle diffusion coefficient is much larger than α_c^2/τ_b , where α_c is the half loss cone angle and τ_b is the bounce period. Under this condition, the mean lifetime of a particle against the pitch angle diffusion into the atmosphere approaches a minimum value that is independent of α_c . This limit is called the strong diffusion limit. In a dipole magnetic field, the value of $D_{\alpha\alpha}\tau_b/\alpha_c^2$ is 0.13 (1.3) at $L = 3$ and 0.46 (4.6) at $L = 4$ for a 50 keV proton with a $D_{\alpha\alpha}$ of 10^{-4} s^{-1} ($=10^{-3} \text{ s}^{-1}$), indicating that the diffusion coefficient of 10^{-4} s^{-1} is close to the strong diffusion limit. Presumably, the loss cone is almost filled when the value $D_{\alpha\alpha}\tau_b/\alpha_c^2$ is close to unity.

[39] According to the formula given by Fok et al. [1993], the Coulomb collision lifetime of a 50 keV proton within the plasmaspheric thermal plasmas becomes comparable to the charge exchange lifetime when the plasmaspheric thermal electron density is $\sim 6 \times 10^4 \text{ cm}^{-3}$ at $L = 2$. An

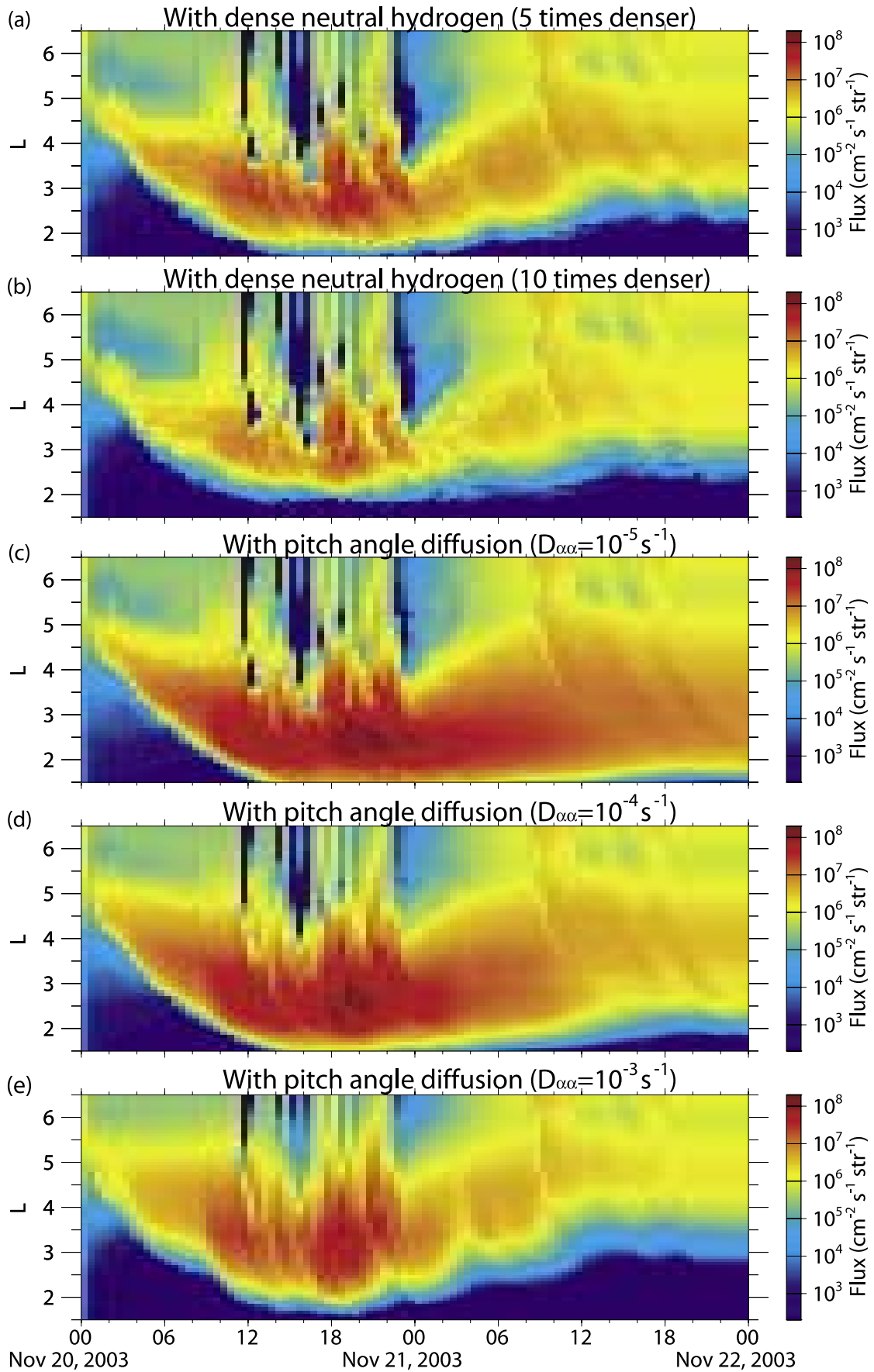


Figure 6

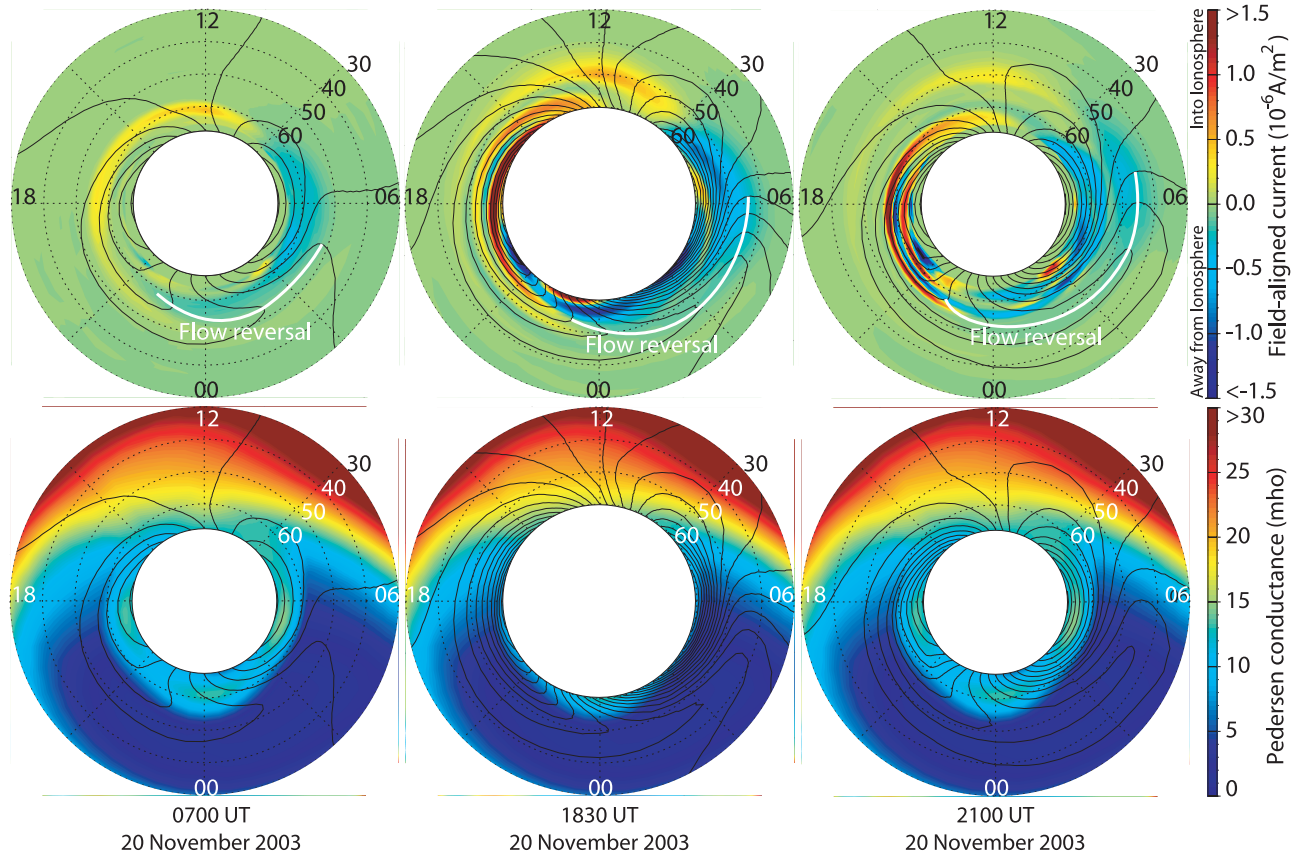


Figure 7. (top) Calculated FAC in the ionosphere at 0700 UT, 1830 UT and 2100 UT on 20 November 2003, and (bottom) the Pedersen conductivity used in the simulation. The downward FAC is indicated with a red color, and the upward FAC is indicated with a blue color. The outer circle corresponds to the 30 MLAT. Electric potential is overlaid with a contour interval of 10 kV.

empirical model of the plasmaspheric density suggested by *Carpenter and Anderson* [1992] predicts a plasmaspheric density of $\sim 2 \times 10^3 \text{ cm}^{-3}$ at $L = 2$. This is an order of magnitude smaller than is necessary to be comparable with the charge exchange lifetime. To account for the rapid retreat of the ion plasma sheet solely on the basis of Coulomb collision, plasmaspheric electrons with densities of 1 or 2 orders of magnitude larger than the modeled densities are needed. However, it is unlikely that the plasmaspheric electron density increases during a large storm, since the plasmasphere is known to be eroded significantly during a large storm due to the enhanced convection electric field.

4.3. Complicated Field-Aligned Current Structure

[40] Figure 7 shows the calculated FAC j_{\parallel} distribution at an ionospheric altitude at 0700 UT (top and left; early main phase), 1830 UT (top and middle; late main phase), and 2100 UT (top and right; early recovery phase). In the early main phase (left), a net downward current flows into the

ionosphere on the duskside, and a net upward currents flows away from the ionosphere on the dawnside. This FAC distribution is consistent with an equatorward portion of the FAC systems statistically obtained by *Zmuda and Armstrong* [1974] and called the Region 2 FAC [*Iijima and Potemra*, 1976]. As the storm develops, there is a general tendency for the Region 2 FAC to expand to lower latitudes and to distort its distribution. In the late main phase (middle), multiple FAC sheets, rather than just two sheets, appear in the premidnight region and on the dayside. The complicated distribution of the FACs remains even in the early recovery phase (right).

[41] Figure 8 shows the calculated FACs at the 2000 MLT meridian on 20–21 November 2003. The red color represents downward FACs (positive j_{\parallel}), and the blue color represents upward FACs (negative j_{\parallel}). During the early main phase (0000–0800 UT), the FAC exhibits a single positive peak indicating an isolated FAC. The upward FAC is not clearly seen in the poleward of the downward FAC since the Region 1 FAC was not specifically included.

Figure 6. Same as Figure 5c except that (a) the geocoronal neutral hydrogen is 5 times denser, (b) the geocoronal neutral hydrogen is 10 times denser, (c) the pitch angle diffusion with its coefficient $D_{\alpha\alpha}$ of 10^{-5} s^{-1} is introduced, (d) the pitch angle diffusion coefficient of 10^{-4} s^{-1} is introduced, and (e) the pitch angle diffusion coefficient of 10^{-3} s^{-1} is introduced.

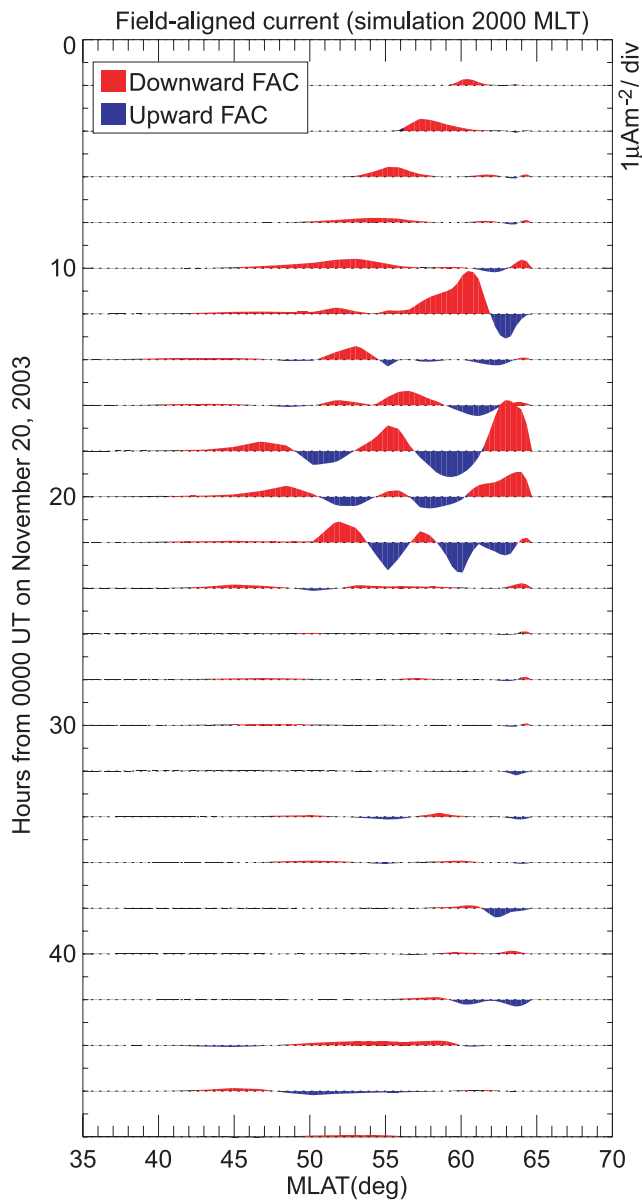


Figure 8. Calculated FAC density at the meridian of 2000 MLT as a function of hours from 0000 UT on 20 November 2003 and magnetic latitude. Downward FAC is indicated with red color, and upward FAC is with blue color.

As the storm proceeds, multiple current sheets, rather than just two sheets, clearly emerge after ~ 1400 UT. This complication is due to changes in the convection electric field and changes in the plasma sheet density, which reflect changes in the plasma pressure distribution in the magnetosphere. In addition, the interchange instability mentioned in the previous section can distort the plasma pressure distribution, resulting in the complicated field-aligned current distribution. The equatorward edge of the FACs moves toward the equator to $\sim 40^\circ$ in the MLAT near a Dst minimum at ~ 1400 UT. When the recovery phase commences, it moves toward the pole, and the FACs almost vanish by 0200 UT on 21 November.

[42] Figure 9 shows the eastward magnetic deflection, ΔB_e , observed by DMSP F16 near the 2000 MLT meridian

in the Northern Hemisphere. If the longitudinal extent of an FAC sheet is much longer than the meridional extent, the density of FAC will be approximately given by

$$j_{||} = \frac{1}{\mu_0} \frac{\Delta B_e}{\Delta l_N} \text{ (positive downward),} \quad (7)$$

where l_N is the line element in the direction of magnetic north [e.g., Iijima and Potemra, 1976]. The important features can be summarized as follows: (1) During the early main phase (0300–0700 UT on 20 November), the FAC shows a single pair of upward and downward FACs; (2) As

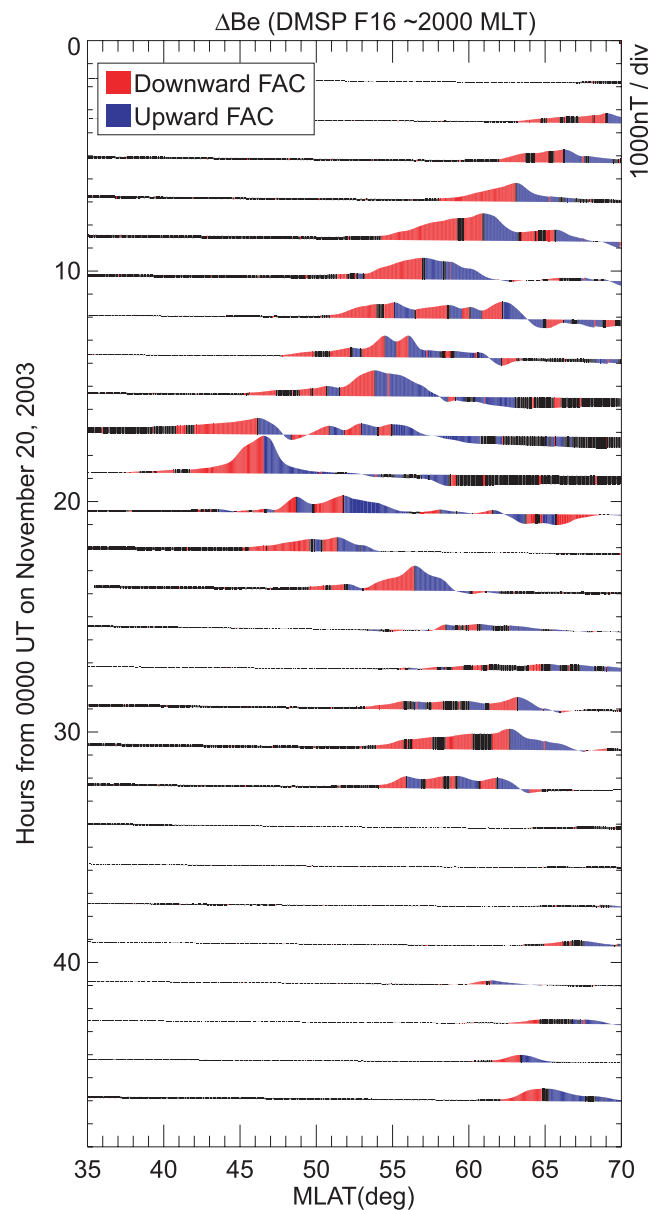


Figure 9. Eastward deflection of the magnetic field ΔB_e observed by DMSP F16 near the meridian of 2000 MLT as a function of hours from 0000 UT on 20 November 2003 and magnetic latitude λ . The red color denotes that $d\Delta B_e/d\lambda > 0$ corresponding to a downward FAC, and the blue color denotes that $d\Delta B_e/d\lambda < 0$ corresponding to an upward FAC.

the storm develops, multiple current sheets, rather than just two sheets, appear in the late main phase (0800–1700 UT); (3) During the main phase (0300–1700 UT), the equatorward edge of the downward FAC moves toward the equator and reaches $\sim 40^\circ$. After that, it starts moving toward the pole; (4) At 0100 UT on 21 November, the intensity of B_e starts decreasing; (5) At 0500 UT on 21 November, the magnitude of B_e is enhanced again, but is weakened by 0900 UT.

[43] The main features of the DMSP observation basically agree with the simulation in terms of the important features from 1 to 4 listed above, although some of the details of the features cannot be simulated. As for item 5, the simulation result does not show an enhancement of the FAC corresponding to the enhancement of B_e between 0500 UT and 0900 UT on 21 November. This disagreement can probably be attributed to the exclusion of the following two mechanisms: (1) changes in N_{ps} and T_{ps} ; and (2) changes in the topology of the magnetic field in the near-Earth tail.

[44] Since no available LANL satellites were located in the nightside sector between 0530 UT and 0800 UT, the values of N_{ps} and T_{ps} were kept constant during this period in the simulation. There is a possibility that N_{ps} was enhanced during this interval, which may explain the intensification of the FAC.

[45] According to the near real-time *AE* index, a substorm expansion took place at about 0540 UT on 21 November, and shortly afterward the *AL* index reached its minimum of about -1400 nT. Substorm activity might modify the plasma pressure distribution on the nightside, as well as the topology of the magnetic field in the tail region. These changes might alter the pressure balance in the nightside region and so change the FAC distribution.

[46] On average, the Region 2 downward FAC is observed to appear in the evening sector equatorward of the Region 1 upward FAC [Iijima and Potemra, 1976]. Watanabe and Iijima [1997] have shown that an additional upward FAC was recorded by the DMSP F7 satellite equatorward of the Region 2 downward FAC in the evening sector during the intense storm of 8 February 1986. A similar feature was observed during the intense storm of 6 April 2000 [Huang and Burke, 2004]. These observations suggest that, during intense storms, the magnetospheric plasma pressure maximizes in the early dusk sector, rather than in the late dusk sector. If the satellite crosses the FAC eastward of the pressure peak, an upward FAC will be observed because of the presence of the westward directed pressure gradient. Returning to the November 2003 storm, the equatorward edge of the FAC sheets is occupied by the downward FAC near the meridian of 2000 MLT, according to the DMSP F16 observation. This morphological feature is consistent with the simulation.

[47] Data from the LANL satellites shows that the N_{ps} distribution was nearly uniform in MLT between the pre-midnight and the postmidnight sectors from 1400 UT to 2000 UT on 20 November 2003 as shown in Figure 1. Before this interval, N_{ps} observed by the 1991-080 satellite in the postmidnight region was higher than that observed by the 1994-084 satellite in the pre-midnight region between 1100 and 1400 UT on 20 November 2003. Given this condition, the plasma pressure in the inner magnetosphere

probably peaked near midnight, rather than in the early dusk region, and hence the upward FAC was probably not located equatorward of the Region 2 downward FAC at the meridian of DMSP F16. This result means that an additional upward FAC does not commonly emerge in the evening sector equatorward of the Region 2 downward FAC during large magnetic storms. FAC geometry may also depend on the local time distribution of the plasma sheet density.

4.4. Ionospheric Flow Reversal at Dawn

[48] The last noticeable feature of the November 2003 storm was the morphology of the convection pattern, noted particularly on the dawnside. The observed zonal flows of the ionospheric plasma during the entire period of this storm are plotted in Figure 10. Figure 10c shows the y -component of the ionospheric plasma flow observed by an Ion Drift Meter on board DMSP F13 on the dawnside in the Southern Hemisphere. The DMSP satellite is a three-axis stabilized spacecraft. The x -axis is along the velocity vector and the z -axis is vertical upward away from the center of the Earth. The y -axis is orthogonal to the xz -plane, as is needed to complete the right-hand system. Since the DMSP F13 is moving poleward on the dawnside in the Southern Hemisphere, the y -component is almost in the eastward direction. The corotation electric field was removed from the original data. The plasma flow is generally eastward at higher latitudes (indicated with the red color) and westward at lower latitudes (indicated with the blue color). Thus there is a region of flow reversal in between. The eastward plasma flow at higher latitudes is most likely driven by the penetration magnetospheric electric field (convection electric field) that is sunward on the dawnside.

[49] A midlatitude westward plasma drift has been observed by the Millstone Hill [Wand and Evans, 1981; Buonsanto et al., 1993], St. Santin [Blanc, 1983], and Arecibo radars [Ganguly et al., 1987], as well as the polar orbiting DE 2 satellite [Heelis and Coley, 1992]. This westward drift is most commonly thought to result from the disturbance wind dynamo [Blanc and Richmond, 1980]. Our data also showed that there was no clear local maximum in the westward drift speed during the main phase as shown in Figure 10c; the westward drift can likely be attributed to the disturbance wind dynamo or some other mechanisms.

[50] During the recovery phase, the westward drift speed had a local maximum of approximately 500 m/s, located about 5° equatorward of the flow reversal between 2200 UT on 20 November and 0200 UT on 21 November. The characteristics of the plasma flow are similar to those reported by Huang et al. [2001], who have shown observations of a sharp ionospheric plasma velocity reversal boundary at midlatitudes during magnetic storms. According to data from the Millstone Hill radar, the zonal plasma drift was eastward (westward) toward the pole (toward the equator) of the velocity reversal boundary between 2100 and 0300 LT. The large westward drift had a local maximum of approximately 500 m/s, located about 2° – 5° equatorward of velocity reversal. Since there was a local maximum of the flow speed, they interpreted the large westward drift in terms of the dawnward extension of the polarization jet electric field (or a rapid subauroral ion drift), rather than the neutral wind dynamo. Such rapid subauroral ion drift is a

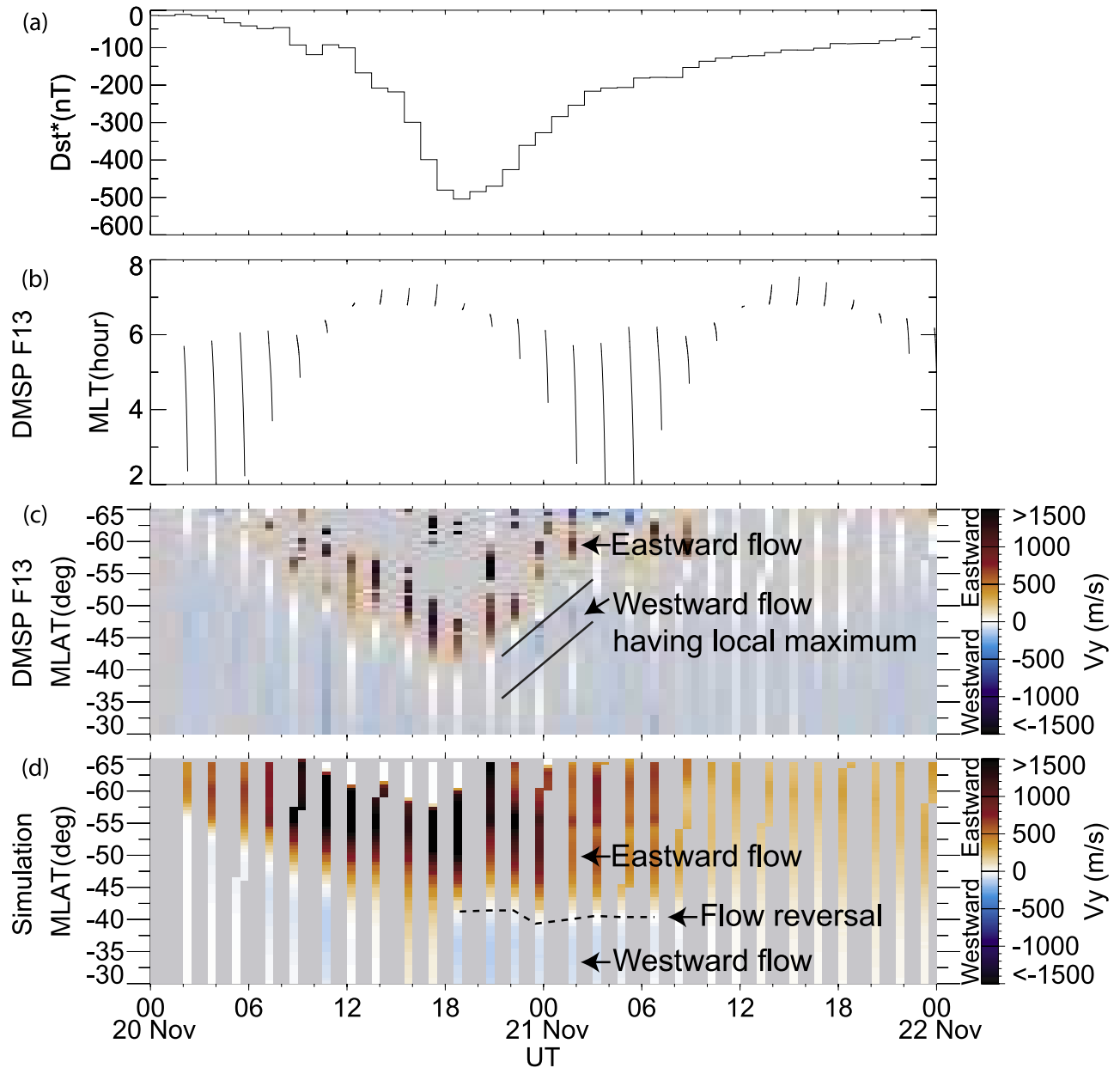


Figure 10. (a) Dst^* , (b) MLT of DMSP F13, (c) y -component (mostly eastward) of the ionospheric plasma drift observed by DMSP F13, and (d) eastward component of the $E \times B$ drift calculated along the DMSP F13 orbit.

well-known phenomenon in the eveningside ionosphere [e.g., Galperin *et al.*, 1974; Anderson *et al.*, 1991].

[51] Our simulation successfully demonstrated that the flow reversal emerges on the dawnside with the presence of a strong Region 2 FACs. Figure 10d shows the zonal component of the $E \times B$ drift calculated along the DMSP F13 orbit, which almost duplicates Figure 10c in terms of the major features. It is clearly seen that the westward drift, located equatorward of the domain of the eastward drift, starts appearing in the late main phase and the recovery phase.

[52] Some of the details of the features cannot be simulated. For example, the simulated reversal does not show a retreat toward the pole during the recovery phase because

the inner edge of the plasma sheet ions does not show a poleward displacement in the simulation as discussed in section 4.2. When the pitch angle diffusion or the dense geocorona was introduced into the simulation, the inner edge of the ion population retreated to high L values, as shown in Figure 6. However, the purpose of the simulation was to demonstrate that the westward plasma drift occurred in the equatorial direction of flow reversal rather than model the poleward retreat.

[53] The simulated pattern of the electric potential is overlaid on the FACs in Figure 7. The flow reversal, marked with a white thick line, is shown to appear over a wide MLT sector extending from premidnight to dawn and over MLATs ranging between 42° and 60° . The easternmost

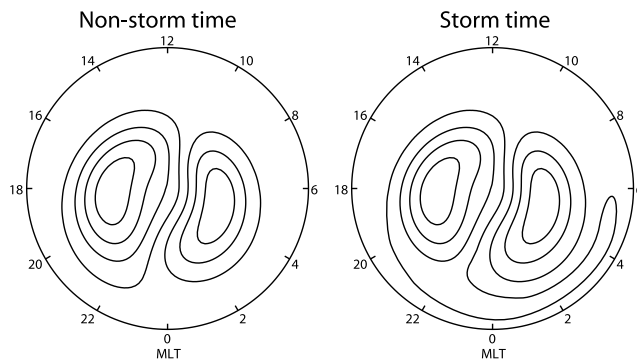


Figure 11. Schematic representation of the storm-time morphology of the ionospheric convection.

edge of the flow reversal tends to move eastward as the storm proceeds, and a part of the duskside convection cell extends to the late morning sector especially during the recovery phase.

[54] Huang *et al.* [2001] attributed the flow reversal to the rapid subauroral ion drift that occurs in most cases in the 1800–0200 MLT sector [Spiro *et al.*, 1979; Karlsson *et al.*, 1998]. The rapid subauroral ion drift is located in the equatorial direction of the high-conductance auroral oval [Anderson *et al.*, 1991] and is associated with a net downward FAC [Rich *et al.*, 1980]. To remove the space charge deposited by the net downward field-aligned current, a strong poleward electric field has to be maintained. Southwood and Wolf [1978] have suggested that this strong poleward electric field drives the observed rapid subauroral ion drift.

[55] As shown in Figure 7, a negative electric potential is associated with the net upward FAC on the dawnside and a positive one associated with the net downward FAC on the duskside. Thus the net potential distribution tends to be canceled out. Consequently, a strong shielding electric field is superposed on the penetration (convection) electric field on the nightside where the conductivity is low. This superposition directly results in a flow reversal on the nightside-morningside boundary. The westward ionospheric plasma drift on the dawnside can be then attributed to the shielding electric field, rather than the eastward extension of the rapid subauroral ion drift because the gap between the downward FAC and the auroral oval is unnecessary. Figure 7 includes the Pedersen conductance distribution used by our simulation, indicating clearly that the westward flow takes place further down in the equatorial direction away from the strong FAC region and the auroral oval.

[56] The morphology of the convection pattern is schematically drawn in Figure 11. During the storm's main phase, the eveningside convection cell was well extended to the morningside due to the strong shielding electric field. The storm-time morphology deviates greatly from the statistical morphology derived from the radar and satellite observations [e.g., Heppner and Maynard, 1987; Weimer, 2001].

5. Conclusion

[57] We have presented the observations and the simulation results of the ring current and associated electrody-

ics that occurred during the superstorm of 20–21 November 2003. The following conclusions can be drawn:

[58] 1. The 20–21 November 2003 storm is the second largest storm (in terms of minimum *Dst*) observed between 1957 and 2004. This storm was unique because of its unusual characteristics including: (1) a polar cap potential drop (at least ~ 200 kV, though likely reaching almost 300 kV); (2) a polar cap boundary ($\sim 60^\circ$ MLAT); and (3) a plasma sheet density of $\sim 5 \text{ cm}^{-3}$ at $L = 6.6$ near the *Dst* minimum.

[59] 2. Both the solar wind density and the plasma sheet density had a similar double peak. If the enhancement of the plasma sheet density was directly associated with that of the solar wind density, the time delay was about 80 min with a correlation coefficient of 0.31. This low correlation coefficient implies that the penetration of the solar wind particles into the magnetosphere is not a simple process. The double peak enhancement of the plasma sheet density is thought to result in the double dips observed in SYM*-H.

[60] 3. Data from the polar-orbiting NOAA 17 shows that the inner edge of the 30–80 keV ions originating from the tail region reached $L \sim 1.5$. This deep penetration can reasonably be explained by the convection electric field based on the Hill-Siscoe-Ober polar cap potential model.

[61] 4. The inner edge of the simulated ion population did not show a rapid retreat to a higher L value during the recovery phase, which is inconsistent with NOAA 17 observations. This disagreement would be reduced if the density of the neutral hydrogen (geocorona) was about 5 times greater than that modeled by Rairden *et al.* [1986], or if the pitch angle diffusion coefficient was equal to or greater than 10^{-4} s^{-1} . A decrease in the plasma sheet density does not account for the retreat of the inner edge to a higher L value. If Coulomb collisions are responsible for the loss of ions, then the plasmaspheric thermal electron density would need to be 1 or 2 orders of magnitude larger than empirical plasmaspheric models suggest.

[62] 5. According to data from DMSP F16, the FACs showed multiple current sheets, rather than just two sheets, during the late main and early recovery phases, which differ from the statistically obtained distribution. This complicated distribution of the FACs can be attributed to a fluctuation in the polar cap potential, a fluctuation in the plasma sheet density, and an interchange instability triggered by a sudden decrease in the plasma sheet density.

[63] 6. The morphology of the convection pattern can be much more complicated than statistically determined due to space charge deposition by the strong Region 2 FACs. Data from DMSP F13 shows that during the early recovery phase, the westward flow speed had a local maximum of approximately 500 m/s about 5° equatorward of the flow reversal. The westward flow can most likely be attributed to the shielding electric field driven by the ring current, rather than the eastward extension of the subauroral ion drift that usually appears in the 1800 and 0200 MLT sector.

[64] **Acknowledgments.** We would like to thank Richard A. Wolf and Robert W. Spiro for their valuable comments and generous support for computation. We also wish to express our gratitude to N. F. Ness and D. J. McComas for providing the ACE data through NSSDC/CDAWeb. The *Dst* and SYM indices were provided by the World Data Center for Geomagnetism, Kyoto, Japan. Y.E. would like to thank Nat Gopalswamy for encouraging the study of the November 2003 superstorm. This work was

supported by the NASA office of Space Science Sun-Earth Connection Guest Investigator Program, under RTOP grant 370-16-00-11.

[65] Arthur Richmond thanks Christophe Peymirat and another reviewer for their assistance in evaluating this paper.

References

- Anderson, P. C., R. A. Heelis, and W. B. Hanson (1991), The ionospheric signatures of rapid subauroral ion drift, *J. Geophys. Res.*, **96**, 5785.
- Bertaux, J. L. (1975), Observed variations of the exospheric hydrogen density with the exospheric temperature, *J. Geophys. Res.*, **80**, 639.
- Bilitza, D. (1997), International Reference Ionosphere-status, 1995/96, *Adv. Space Res.*, **20**, 1751.
- Blanc, M. (1983), Magnetospheric convection effects at midlatitudes: 3. Theoretical derivation of the disturbance convection pattern in the plasmasphere, *J. Geophys. Res.*, **88**, 235.
- Blanc, M., and A. D. Richmond (1980), The ionospheric disturbance dynamo, *J. Geophys. Res.*, **85**, 1669.
- Borovsky, J. E., M. F. Thomsen, and R. C. Elphic (1998), The driving of the plasma sheet by the solar wind, *J. Geophys. Res.*, **103**, 17,617.
- Boyle, C. B., P. H. Reiff, and M. R. Hairston (1997), Empirical polar cap potentials, *J. Geophys. Res.*, **102**, 111.
- Buonsanto, M. J., M. E. Hagan, J. E. Salah, and B. J. Fejer (1993), Solar cycle and seasonal variations in *F* region electrodynamics at Millstone Hill, *J. Geophys. Res.*, **98**, 15,677.
- Carpenter, D. L., and R. R. Anderson (1992), An ISEE/whistler model of equatorial electron density in the magnetosphere, *J. Geophys. Res.*, **97**, 1097.
- Chamberlain, J. W. (1963), Planetary coronae and atmospheric evaporation, *Planet. Space Sci.*, **11**, 901.
- Chen, M. W., L. R. Lyons, and M. Schulz (1994), Simulations of phase space distributions of storm time proton ring current, *J. Geophys. Res.*, **99**, 5745.
- Chen, M. W., J. L. Roeder, J. F. Fennell, L. R. Lyons, R. L. Lambour, and M. Schulz (1999), Proton ring current pitch angle distributions: Comparison of simultaneous simulations with CRRES observations, *J. Geophys. Res.*, **104**, 17,379.
- Daglis, I. A. (1997), The role of magnetosphere-ionosphere coupling in magnetic storm dynamics, in *Magnetic Storms, Geophys. Monogr. Ser.*, vol. 98, edited by B. T. Tsurutani et al., p. 107, AGU, Washington, D. C.
- Dessler, A. J., and E. N. Parker (1959), Hydrodynamic theory of geomagnetic storms, *J. Geophys. Res.*, **64**, 2239.
- Ebihara, Y., and M. Ejiri (1998), Modeling of solar wind control of the ring current buildup: A case study of the magnetic storms in April 1997, *Geophys. Res. Lett.*, **25**, 3751.
- Ebihara, Y., and M. Ejiri (2000), Simulation study on fundamental properties of the storm-time ring current, *J. Geophys. Res.*, **105**, 15,843.
- Ebihara, Y., and M. Ejiri (2003), Numerical simulation of the ring current: Review, *Space Sci. Rev.*, **105**(1–2), 377.
- Ebihara, Y., M.-C. Fok, R. A. Wolf, T. J. Immel, and T. E. Moore (2004), Influence of ionosphere conductivity on the ring current, *J. Geophys. Res.*, **109**, A08205, doi:10.1029/2003JA010351.
- Fok, M.-C., and T. E. Moore (1997), Ring current modeling in a realistic magnetic field configuration, *Geophys. Res. Lett.*, **24**, 1775.
- Fok, M.-C., J. U. Kozyra, A. F. Nagy, C. E. Rasmussen, and G. V. Khazanov (1993), Decay of equatorial ring current ions and associated aeronomical consequences, *J. Geophys. Res.*, **98**, 19,381.
- Fok, M.-C., R. A. Wolf, R. W. Spiro, and T. E. Moore (2001), Comprehensive computational model of Earth's ring current, *J. Geophys. Res.*, **106**, 8417.
- Fok, M.-C., et al. (2003), Global ENA image simulations, *Space Sci. Rev.*, **109**, 77.
- Galperin, Y., V. N. Ponomarev, and A. G. Zosimova (1974), Plasma convection in the polar ionosphere, *Ann. Geophys.*, **30**, 1.
- Ganguly, S., R. A. Behnke, and B. A. Emery (1987), Average electric field behavior in the ionosphere above Arecibo, *J. Geophys. Res.*, **92**, 1199.
- Garner, T. W., R. A. Wolf, R. W. Spiro, W. J. Burke, B. G. Fejer, S. Sazykin, J. L. Roeder, and M. R. Hairston (2004), Magnetospheric electric fields and plasma sheet injection to low L-shells during the 4–5 June 1991 magnetic storm: Comparison between the Rice Convection Model and observations, *J. Geophys. Res.*, **109**, A02214, doi:10.1029/2003JA010208.
- Gonzalez, W. D., J. A. Joselyn, Y. Kamide, H. W. Kroehl, G. Rostoker, B. T. Tsurutani, and V. M. Vasyliunas (1994), What is a geomagnetic storm?, *J. Geophys. Res.*, **99**, 5771.
- Hairston, M. R., T. W. Hill, and R. A. Heelis (2003), Observed saturation of the ionospheric polar cap potential during the 31 March 2001 storm, *Geophys. Res. Lett.*, **30**(6), 1325, doi:10.1029/2002GL015894.
- Hardy, D. A., M. S. Gussenhoven, R. Raistrick, and W. J. McNeil (1987), Statistical and functional representations of the pattern of auroral energy flux, number flux, and conductivity, *J. Geophys. Res.*, **92**, 12,275.
- Harel, M., R. A. Wolf, P. H. Reiff, R. W. Spiro, W. J. Burke, F. J. Rich, and M. Smiddy (1981), Quantitative simulation of a magnetospheric substorm: 1. Model logic and overview, *J. Geophys. Res.*, **86**, 2217.
- Hedin, A. E. (1991), Extension of the MSIS thermospheric model into the middle and lower atmosphere, *J. Geophys. Res.*, **96**, 1159.
- Heelis, R. A., and W. R. Coley (1992), East-west ion drifts at midlatitudes observed by Dynamics Explorer 2, *J. Geophys. Res.*, **97**, 19,461.
- Heppner, J. P., and N. C. Maynard (1987), Empirical high-latitude electric field models, *J. Geophys. Res.*, **92**, 4467.
- Hill, T. W., A. J. Dessler, and R. A. Wolf (1976), Mercury and Mars: The role of ionospheric conductivity in the acceleration of magnetospheric particles, *Geophys. Res. Lett.*, **3**, 429.
- Huang, C. Y., and W. J. Burke (2004), Transient sheets of field-aligned current observed by DMSP during the main phase of a magnetic superstorm, *J. Geophys. Res.*, **109**, A06303, doi:10.1029/2003JA010067.
- Huang, C. S., J. C. Foster, and J. M. Holt (2001), Westward plasma drift in the midlatitude ionospheric region in the midnight-dawn sector, *J. Geophys. Res.*, **106**, 30,349.
- Iijima, T., and T. A. Potemra (1976), The amplitude distribution of field-aligned currents at northern high latitudes observed by Triad, *J. Geophys. Res.*, **81**, 2165.
- Jordanova, V. K., C. J. Farrugia, L. Janoo, J. M. Quinn, R. B. Torbert, K. W. Ogilvie, R. P. Lepping, J. T. Steinberg, D. J. McComas, and R. D. Belian (1998), October 1995 magnetic cloud and accompanying storm activity: Ring current evolution, *J. Geophys. Res.*, **103**, 79.
- Jordanova, V. K., C. J. Farrugia, J. M. Quinn, R. B. Torbert, J. E. Borovsky, R. B. Sheldon, and W. K. Peterson (1999a), Simulation of off-equatorial ring current ion spectra measured by Polar for a moderate storm at solar minimum, *J. Geophys. Res.*, **104**, 429.
- Jordanova, V. K., R. B. Torbert, R. M. Thorne, H. L. Collin, J. L. Roeder, and J. C. Foster (1999b), Ring current activity during the early $B_z < 0$ phase of the January 1997 magnetic cloud, *J. Geophys. Res.*, **104**, 24,895.
- Jordanova, V. K., C. J. Farrugia, R. M. Thorne, G. V. Khazanov, G. D. Reeves, and M. F. Thomsen (2001a), Modeling ring current proton precipitation by electromagnetic ion cyclotron waves during the May 14–16, 1997, storm, *J. Geophys. Res.*, **106**, 7.
- Jordanova, V. K., L. M. Kistler, C. J. Farrugia, and R. B. Torbert (2001b), Effects of inner magnetospheric convection on ring current dynamics: March 10–12, 1998, *J. Geophys. Res.*, **106**, 29,705.
- Jordanova, V. K., R. M. Thorne, C. J. Farrugia, Y. Dotan, J. F. Fennell, M. F. Thomsen, G. D. Reeves, and D. J. McComas (2001c), Ring current dynamics during the 13–18 July 2000 storm period, *Solar Phys.*, **204**, 361.
- Jordanova, V. K., A. Boonsirirath, R. M. Thorne, and Y. Dotan (2003), Ring current asymmetry from global simulations using a high-resolution electric field model, *J. Geophys. Res.*, **108**(A12), 1443, doi:10.1029/2003JA009993.
- Karlsson, T., G. T. Marklund, L. G. Blomberg, and A. Malkki (1998), Subauroral electric fields observed by the Freja satellite: A statistical study, *J. Geophys. Res.*, **103**, 4327.
- Kennel, C. F. (1969), Consequences of a magnetospheric plasma, *Rev. Geophys.*, **7**, 379.
- Khazanov, G. V., K. V. Gamayunov, and V. K. Jordanova (2003a), Self-consistent model of magnetospheric ring current and electromagnetic ion cyclotron waves: The 2–7 May 1998 storm, *J. Geophys. Res.*, **108**(A12), 1419, doi:10.1029/2003JA009856.
- Khazanov, G. V., M. W. Liemohn, T. S. Newman, M.-C. Fok, and R. W. Spiro (2003b), Self-consistent magnetosphere-ionosphere coupling: Theoretical studies, *J. Geophys. Res.*, **108**(A3), 1122, doi:10.1029/2002JA009624.
- Kozyra, J. U., M.-C. Fok, E. R. Sanchez, D. S. Evans, D. C. Hamilton, and A. F. Nagy (1998a), The role of precipitation losses in producing the rapid early recovery phase of the great magnetic storm of February 1986, *J. Geophys. Res.*, **103**, 6801.
- Kozyra, J. U., V. K. Jordanova, J. E. Borovsky, M. F. Thomsen, D. J. Knipp, D. S. Evans, D. J. McComas, and T. E. Cayton (1998b), Effects of a high-density plasma sheet on ring current development during the November 2–6, 1993, *J. Geophys. Res.*, **103**, 26,285.
- Kozyra, J. U., M. W. Liemohn, C. R. Clauer, A. J. Ridley, M. F. Thomsen, J. E. Borovsky, J. L. Roeder, V. K. Jordanova, and W. D. Gonzalez (2002), Multistep *Dst* development and ring current composition changes during the 4–6 June 1991 magnetic storm, *J. Geophys. Res.*, **107**(A8), 1224, doi:10.1029/2001JA000023.
- Liemohn, M. W., J. U. Kozyra, V. K. Jordanova, G. V. Khazanov, M. F. Thomsen, and T. E. Cayton (1999), Analysis of early phase ring current recovery mechanisms during magnetic storms, *Geophys. Res. Lett.*, **26**, 2845.

- Liemohn, M. W., J. U. Kozyra, M. F. Thomsen, J. L. Roeder, G. Lu, J. E. Borovsky, and T. E. Cayton (2001), Dominant role of the asymmetric ring current in producing the stormtime Dst^* , *J. Geophys. Res.*, **106**, 10,883.
- Liemohn, M. W., J. U. Kozyra, C. R. Clauer, G. V. Khazanov, and M. F. Thomsen (2002a), Adiabatic energization in the ring current and its relation to other source and loss terms, *J. Geophys. Res.*, **107**(A4), 1045, doi:10.1029/2001JA000243.
- Liemohn, M. W., J. U. Kozyra, M. R. Hairston, D. R. Weimer, G. Lu, A. J. Ridley, T. H. Zurbuchen, and R. M. Skoug (2002b), Consequences of a saturated convection electric field on the ring current, *Geophys. Res. Lett.*, **29**(9), 1348, doi:10.1029/2001GL014270.
- McComas, D., S. Bame, B. Barraclough, J. Donart, R. Elphic, J. Gosling, M. Moldwin, K. Moore, and M. F. Thomsen (1993), Magnetospheric plasma analyzer: Initial three spacecraft observations from geosynchronous orbit, *J. Geophys. Res.*, **98**, 13,453.
- Ober, D. M., N. C. Maynard, and W. J. Burke (2003), Testing the Hill model of transpolar potential saturation, *J. Geophys. Res.*, **108**(A12), 1467, doi:10.1029/2003JA010154.
- Rairden, R. L., L. A. Frank, and J. D. Craven (1986), Geocoronal imaging with Dynamics Explorer, *J. Geophys. Res.*, **91**, 13,613.
- Rich, F. J., W. J. Burke, M. C. Kelley, and M. Smiddy (1980), Observations of field-aligned currents in association with strong convection electric fields at subauroral latitudes, *J. Geophys. Res.*, **85**, 2335.
- Sazykin, S., R. A. Wolf, R. W. Spiro, T. I. Gombosi, D. L. De Zeeuw, and M. F. Thomsen (2002), Interchange instability in the inner magnetosphere associated with geosynchronous particle flux decreases, *Geophys. Res. Lett.*, **29**(10), 1448, doi:10.1029/2001GL014416.
- Sckopke, N. (1966), A generation relation between the energy of trapped particles and the disturbance field near the earth, *J. Geophys. Res.*, **71**, 3125.
- Sheldon, R. B., and D. C. Hamilton (1993), Ion transport and loss in the Earth's quiet ring current, 1, Data and standard model, *J. Geophys. Res.*, **98**, 13,491.
- Siscoe, G. L., G. M. Erickson, B. U. Ö. Sonnerup, N. C. Maynard, J. A. Schoendorf, K. D. Siebert, D. R. Weimer, W. W. White, and G. R. Wilson (2002), Hill model of transpolar potential saturation: Comparisons with MHD simulations, *J. Geophys. Res.*, **107**(A6), 1075, doi:10.1029/2001JA000109.
- Southwood, D. J., and R. A. Wolf (1978), An assessment of the role of precipitation in magnetospheric convection, *J. Geophys. Res.*, **85**, 5227.
- Spiro, R. W., R. A. Heelis, and W. B. Hanson (1979), Rapid subauroral ion drifts observed by Atmosphere Explorer C, *Geophys. Res. Lett.*, **6**, 657.
- Thomsen, M. F., J. E. Borovsky, D. J. McComas, and M. B. Moldwin (1996), Observations of the Earth's plasma sheet at geosynchronous orbit, in *Workshop on the Earth's Trapped Particle Environment, AIP Conf. Proc.*, **383**, 25.
- Tinsley, B. A., R. R. Hodges Jr., and R. P. Rohrbaugh (1986), Monte Carlo models for the terrestrial exosphere over a solar cycle, *J. Geophys. Res.*, **91**, 13,631.
- Toffoletto, F., S. Sazykin, R. Spiro, and R. Wolf (2003), Inner magnetospheric modeling with the Rice Convection Model, *Space Sci. Rev.*, **107**, 175.
- Tsyganenko, N. A. (1995), Modeling the Earth's magnetospheric magnetic field confined within a realistic magnetopause, *J. Geophys. Res.*, **100**, 5599.
- Tsyganenko, N. A., and D. P. Stern (1996), A new-generation global magnetosphere field model, based on spacecraft magnetometer data, *ISTP Newsl.*, **6**(1), 21.
- Wand, R. H., and J. V. Evans (1981), Seasonal and magnetic activity variations of ionospheric electric fields over Millstone Hill, *J. Geophys. Res.*, **86**, 103.
- Watanabe, M., and T. Iijima (1997), Nightside subauroral field-aligned current system during great magnetic storms, *Proc. NIPR Symp. Upper Atmos. Phys.*, **10**, 135.
- Weimer, D. R. (2001), An improved model of ionospheric electric potentials including substorm perturbations and application to the Geospace Environment Modeling November 24, 1996, event, *J. Geophys. Res.*, **106**, 407.
- Zmuda, A. J., and J. C. Armstrong (1974), The diurnal flow pattern of field-aligned currents, *J. Geophys. Res.*, **79**, 4611.

Y. Ebihara and M. Ejiri, National Institute of Polar Research, 1-9-10 Kaga, Itabashi-ku, Tokyo 173-8515, Japan. (ebihara@nipr.ac.jp; ejiri@nipr.ac.jp)

D. S. Evans, NOAA Space Environment Laboratory, 325 Broadway, Boulder, CO 80303, USA. (david.s.evans@noaa.gov)

M.-C. Fok, NASA Goddard Space Flight Center, Code 612.2, Greenbelt, MD 20771, USA. (mei-ching.h.fok@nasa.gov)

M. R. Hairston, Center for Space Science, University of Texas at Dallas, P. O. Box 830688, F022, Richardson, TX 75083-0688, USA. (hairston@utdallas.edu)

F. J. Rich, Air Force Research Laboratory, AFRL/VSBXP 29, Hanscom Air Force Base, MA 01731-3010, USA. (frederick.rich@hanscom.af.mil)

S. Sazykin, Physics and Astronomy Department, Rice University, MS 108, 6100 S. Main Street, Houston, TX 77005-1892, USA. (sazykin@rice.edu)

M. F. Thomsen, Los Alamos National Laboratory, MS D466, Los Alamos, NM 87545, USA. (mthomsen@lanl.gov)